Materials Characterization 225 (2025) 115205

Contents lists available at ScienceDirect

Materials Characterization

journal homepage: www.elsevier.com/locate/matchar

Elucidating deformation behavior of cementite and κ-carbide during friction stir welding of Fe-0.1C-xAl (x = 0.05 and 5 mass%) steels below A_1

Junqi Chen, Takuya Miura, Kohsaku Ushioda, Hidetoshi Fujii *

Joining and Welding Research Institute (JWRI), Osaka University, 11-1 Mihogaoka, Ibaraki, Osaka, Japan

ARTICLE INFO

Keywords:
Fe-0.1C-xAl ferrite steel
Friction stir welding
Cementite
κ-carbide deformation

ABSTRACT

The deformation behavior of cementite and κ-carbide of Fe-0.1C-0.05Al and Fe-0.1C-5Al (mass%) steels at below A_1 friction stir welding (FSW) was investigated. Quantitative nano-hardness measurements revealed that cementite exhibited high hardness (13.0 GPa) and strong resistance to deformation (0.22 μN/nm^2), whereas κ-carbide had a lower hardness of 6.9 GPa and resistance force of 0.083 μN/nm^2 for the first time. During FSW under an axial load of 40 kN at a rotation rate of 80 rpm (peak temperatures ~700 °C, below A_1), few dislocations were introduced into the structure of cementite, which is hard and brittle and is prone to fragmentation owing to the accumulation of dislocations at the ferrite/cementite interface. In contrast, κ-carbides, being softer, exhibited considerable plastic deformation and were presumed to be sheared by the high-density dislocations introduced under the same conditions. The shear processing plausibly triggers dynamic redistribution of the C atoms, where dislocations penetrate through the κ-carbides, disrupting Fe—C bonding. These phenomena enable the transfer of C atoms from the κ-carbides to the matrix and subsequent precipitation of fine cementite along part of the grain boundaries during the cooling stage after FSW. Furthermore, the introduced dislocations remain within the shearable κ-carbides and may serve as dislocation sources in subsequent deformation processes, thereby enhancing the ductility of the steels. The present study is the first to clearly reveal the internal dislocation features of carbides and analyze the distinct deformation behavior of different carbides during FSW below A_1.

1. Introduction

Ferrite-based Fe-C-Al lightweight steels, known for their exceptional specific strength, have attracted significant attention for applications in lightweight ground transportation systems, such as automobiles and heavy trucks [1–3]. Increasing the Al content is an effective approach for reducing the weight of the structural components [4], because the atomic weight of Al is lower (26.981) and the atomic radius (143 pm) is larger than the atomic weight (55.847) and atomic radius (124 pm) of Fe. This achievement originates from lattice expansion and lowers the average molar mass of the steel [5,6]. High-Al ferritic steels boost automotive fuel efficiency and offer excellent corrosion resistance for ship hulls and offshore structures in marine environments, promoting growth of the green economy [7–9].

The addition of alloying elements significantly influences the microstructure and phase composition of alloy systems, thereby promoting the precipitation of new secondary phases. In Fe-C-Al alloys, the precipitated carbides may consist of cementite, κ-carbides, or a combination of both with different Al and C contents. According to the Fe—C binary phase diagram, the primary phases in carbon steels are ferrite (α-Fe) and carbides, where θ-type Fe_3C (cementite) carbide is the most recognized, having an orthorhombic crystal structure in the Pnma space group [10,11]. The addition of Al to the Fe—C system significantly affects the phase fields and phase constituents. Adding C and Al to steel reduces the stability of cementite and promotes the formation of κ-carbides [12]. At Al contents greater than 2 mass%, κ-carbides with a perovskite-like $L1_2$ cubic crystal structure in the Pm3m space group are introduced, and the volume fraction increases with increasing C content [13]. κ-carbides, represented by the formula Fe_3AlC_x (where x ranges from 0.5 to 1), have a lattice parameter that varies from 0.372 to 0.379 nm as the C concentration increases [14]. Previous studies [15] have reported that alloys with 7 mass% Al and C contents of 2–2.5 mass% consist of ferrite and κ-carbides, without cementite. When the C content is in the range of 2.7–4 mass%, the matrix includes ferrite, κ-carbide, and cementite. This shift is attributed to the excess C, which promotes the formation of cementite, with a high C content potentially leading to the

* Corresponding author.
E-mail address: fujii.hidetoshi.jwri@osaka-u.ac.jp (H. Fujii).

https://doi.org/10.1016/j.matchar.2025.115205
Received 18 March 2025; Received in revised form 20 May 2025; Accepted 20 May 2025
Available online 22 May 2025

formation of graphite. A recent study [16] discussed Fe-1.2C-1.5Cr-5Al (mass%) low-density steel for bearings, in which the addition of 5 mass % Al led to the precipitation of κ-carbides. Consequently, κ-carbides and cementite coexisted with α-Fe in the eutectoid microstructure.

Carbide precipitation is a key mechanism for strengthening alloys. Controlling the deformation behavior of carbides during severe plastic deformation (SPD) is expected to be an effective strategy for achieving high strength or an optimal strength-ductility balance. Cementite is generally considered detrimental to the ductility and toughness of steel owing to its brittle nature, particularly when present as coarse cementite [17,18]. Fe-0.1C-0.05Al alloys containing cementite particles of approximately 2 μm in size exhibited reduced ductility and toughness, where the coarse cementite hindered dislocation movement during deformation and caused notable stress concentration [19]. On the other hand, Li et al. [20] reported the fabrication of ultrahigh-strength nanostructured materials by drawing pearlitic steel with thin lamella cementite. Under high strain, thin cementite dissolves via mechanical alloying, transforming the pearlitic structure into a C-saturated iron phase with subgrain sizes of ~10 nm, leading to an extremely high tensile strength of 7 GPa and making the alloy the most ductile bulk material known. Sauvage et al. [21] reported the dissolution behavior of cementite in pearlitic steels during high-pressure torsion (HPT). Under severe torsion, the lamellar Fe_3C elongates, fragments, and C atoms in Fe_3C near the phase boundary migrate to dislocations in the ferrite, creating vacancies and a thin off-stoichiometric Fe_3C layer. Subsequently, some of these C atoms diffuse along the dislocation cores, accumulating at the Fe_3C/α-Fe interface. With increasing strain, the dislocation cells in ferrite trap C atoms, leading to gradual cementite decomposition. With five torsions (N = 5), only Fe_3C nanoclusters remained, indicating that vacancies played a key role in carbide dissolution [21].

κ-carbides may exhibit varied responses. Yao et al. [22] observed that nano-sized κ-carbide precipitation led to a notable increase in the yield strength of high-Mn mild steel (~480 MPa) without considerably sacrificing tensile elongation. Furthermore, studies have demonstrated that κ-carbides for which morphology was optimized through appropriate thermomechanical treatment (TMT) acted as a strengthening phase in high-C (0.3–1.1 wt%), lightweight ferritic steels, without significant ductility loss [12,23]. Therefore, during plastic deformation, κ-carbides in the Fe-Al-C ternary system are expected to improve the mechanical properties by replacing cementite [24], whereas brittle carbides such as cementite with low strain energy [25] can lead to both precipitation strengthening and ductility loss.

Precipitated phases are a key source of strengthening, and their evolution during deformation significantly affects the material properties such as strength, ductility, and toughness. Therefore, understanding the behavior of cementites and κ-carbides during deformation is novel enough to be crucial for the development of low-density, highly corrosion-resistant Fe-C-Al alloys with superior performance to meet growing industrial demands. In terms of structural applications, friction stir welding (FSW) [26] shows great promise for achieving severe plastic deformations, such as equal channel angular extrusion (ECAE) [27], severe plastic torsion straining (SPTS) [28], and accumulative roll bonding (ARB) [29]. Research by the present authors has demonstrated for the first time that during FSW, the κ-carbides present in Fe-0.1C-5Al base metal surprisingly transform into finer κ-carbides and a semi-network of ultrafine cementite, resulting in increased alloy strength, alongside improved ductility and toughness [19].

In general, as a solid-phase welding method [26], FSW presents a promising solution to the common welding problems (cracking susceptibility) faced by high-Al steels. Controlling the parameters (rotation rate: 80 rpm; transverse speed: 100 mm/min; axial force 40 kN) can enable effective joining of the alloy at a peak welding temperature below A_1 (joining without phase transformation) [19,30], ensuring that the material retains the excellent multifaceted properties of ferrite-based, high-Al alloys. In addition, FSW refines the grains through dynamic recrystallization at elevated temperatures [31], overcoming the issue of coarse grains typically observed in Fe—Al steels owing to the lack of phase transformation during the cooling stage of production [15], thus achieving the desired combination of strength and toughness in the stir zone (SZ) region. Moreover, the simultaneous thermo-mechanical effects unique to FSW induce distinct deformation behaviors of cementite and κ-carbide, potentially enhancing the mechanical properties. Currently, investigations on the FSW of ferrite Fe-C-Al solid-solution alloys with Al as the principal alloying element are scarce. Even fewer studies have considered the presumably different deformation behaviors of precipitated carbides with varying Al contents. However, direct evidence of the deformation behavior of carbides is novel and challenging to obtain, with crack rupture along certain fracture surfaces serving as one of the few macroscopically visible indicators, and recorded instances being extremely limited.

The complexity of ternary or multicomponent alloy systems may obscure analysis of the structure and deformation mechanisms of carbides. Thus, simpler ternary Fe-C-Al alloys are more suitable and valuable as target alloys. This study systematically evaluates the deformation behavior of cementite and κ-carbides during FSW of Fe-0.1C-0.05Al and Fe-0.1C-5Al (mass%) steels at temperatures below A_1 by monitoring the internal dislocation characteristics of the deformed carbides.

2. Materials and methodology

2.1. Material preparation

Fe-0.1C-0.05Al and Fe-0.1C-5Al alloy ingots were prepared via vacuum induction melting. The chemical compositions of the target alloys are listed in Table 1. The processing routes for hot rolling and subsequent annealing are illustrated in Fig. 1. Initially, the steel ingots were preheated to 700 °C and subjected to multiple hot-rolling passes. After each pass, the ingots were reheated at 700 °C for 10 min before proceeding to the next pass until the sheet thickness reached 3.4 mm. After hot rolling, the sheets were annealed at 700 °C for 30 min and air-cooled. The oxidized layers were removed from the top and bottom surfaces using a milling machine to a final thickness of 3.0 mm; this served as the starting material for FSW.

As shown in Fig. 2, in the FSW process, the peak temperature was maintained at approximately 700 °C in the ferrite region according to our previous study [19]. The welding parameters were as follows: rotation rate of 80 rpm, traverse speed of 100 mm/min, and an axial force of 40 kN. The FSW tool was composed of cemented tungsten carbide (WC) (FSW7; Sanalloy, Japan). The shoulder diameter, probe diameter, and probe length were 15, 6, and 2.9 mm, respectively. The tool was tilted at an angle of 3° relative to the rotational axis in the transverse direction. Ar was used as the shielding gas at a flow rate of 20 L/min during welding.

2.2. Microstructural investigations

The specimens for microstructural analysis were sectioned using linear motor-operated wire electrical discharge machining (EDM; Sodick AG360L). Microstructural observations were performed using field-emission scanning electron microscopy (FE-SEM, JEOL JSM-7001FA), transmission electron microscopy (TEM, JEOL 2011F), and electron probe microanalysis (EPMA, JEOL JXA-8530F). The SEM and EPMA

Table 1
Main chemical composition of the steels (mass%) and A_{e1} (°C) temperatures calculated with Thermo-Calc using the TCFE9 database.

Type	C	Al	Fe	A_{e1}
Fe-0.1C-0.05Al	0.11	0.033	Bal.	727
Fe-0.1C-5Al	0.11	5.27	Bal.	766

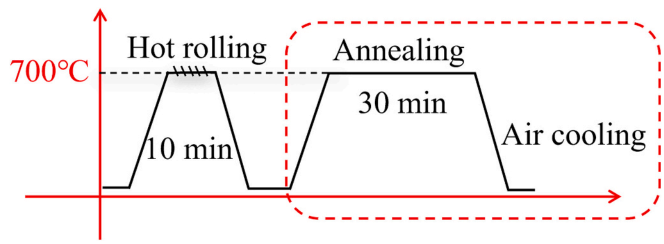

Fig. 1. Schematic of hot rolling and subsequent annealing conditions for Fe-0.1C-0.05Al and Fe-0.1C-5Al steels.

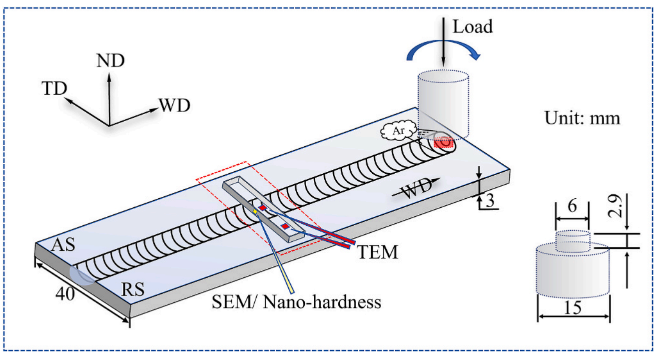

Fig. 2. Welding procedure, geometric dimensions of the tool (unit: mm), and selected location for SEM/TEM/nano-hardness specimens, respectively.

specimens were mechanically polished and etched using a 4.0 % nitric acid +96.0 % ethanol solution. The TEM specimens were fabricated using focused ion beam (FIB; FB-2000s Hitachi) milling, targeting the central region of the SZ, as indicated by the red box in Fig. 2.

2.3. Nano-hardness test

The nano-hardness experiments were carried out using a nano-indentation machine (Bruker-Hysitron TI Premier) equipped with a computer-controlled indentation system that continuously monitors the displacement (h) of the tip of the Berkovich-type diamond indentation head and the applied load (P) throughout the test. The P-h curve was analyzed based on the continuous stiffness method [32]. The nano-hardness of the carbides was measured by setting the peak load at 800 μN. Special attention was paid to ensure that carbides reaching more than three times the size of the indentation were selected to avoid interference from the matrix.

3. Results and discussion

3.1. Microstructures

Fig. 3a1,c1 displays the SEM images after etching the initial microstructures of Fe-0.1C-0.05Al and Fe-0.1C-5Al prior to FSW, respectively. The microstructures of the SZs after FSW below A_1 are shown in Fig. 3b1 and d1. Here, wavelength dispersive spectroscopy (WDS) microanalysis using EPMA was employed to investigate the distribution of C and Al to distinguish between cementite and κ-carbide. The C distribution is presented in Fig. 3a2,b2 and c2,d2, whereas Fig. 3a3,b3 and c3,d3 show the Al distribution. All thermal processing was performed within the range of existence of the single ferrite phase, without the $\alpha \rightarrow \gamma$ phase transformation. The initial grain sizes of ferrite in both steel plates were relatively coarse and inhomogeneous owing to the lack of homogenization heat treatment. The size of the cementites in the base metal (BM) of Fe-0.1C-0.05Al was approximately 1.7 μm. In contrast, with the addition of 5 mass% Al, the carbide type was converted from cementite to κ-carbide, as revealed by EPMA (Fig. 3a3,c3), and ferrite coexisted with smaller κ carbides ($d_{ave.} \approx 0.6$ μm) in the microstructure of the BM in the Fe-0.1C-5Al specimens, without cementite. κ-carbides exist within an appreciable ternary homogeneity range in the Fe-Al-C system [33]. The authors' previous report verified the presence of κ-carbides from the TEM images and Kikuchi patterns using scanning electron microscopy-electron backscatter diffraction (SEM-EBSD) [19]. In addition to the grain refinement caused by dynamic recrystallization during the FSW process [34], intense plastic deformation may cause partial fragmentation of cementite in the BM of Fe-0.1C-0.05Al, as evidenced by the presence of broken cementite in the SZ (Fig. 3e), producing slightly smaller cementite (avg. size of ~1.4 μm), without other types of carbide. The slight reduction in the average size of the cementite is likely attributed to the dynamic relaxation of high stress-concentrations at the interface between cementite and the matrix. This relaxation is caused by the accumulation of dislocations during FSW at ~700 °C, leading to a reduced frequency of cementite fracture compared to that observed at room temperature or lower temperatures, such as during tensile or Charpy impact testing [19]. Furthermore, the shape of cementite may influence its fragmentation behavior. The lamellar cementite in pearlite was easily fragmented during FSW below the A_1 temperature [35], whereas fragmentation of globular cementite was difficult. In contrast, for Fe-0.1C-5Al, a significant portion of κ-carbides in the BM surprisingly dissolved, and the retained portion was refined to an average size of 0.4 μm in the SZ. In addition, newly precipitated cementite, approximately 0.2 μm in size, was observed along the grain boundaries, with a semi-reticulated shape, as indicated in the marked regions in Fig. 3d1. The above analyses revealed two distinct carbides, differing in morphology, size, and chemical composition, and highlights their evolution during FSW.

3.2. Mechanical properties of SZs

Fig. 4 presents a spider chart comparing the mechanical properties of the SZs of Fe-0.1C-0.05Al and Fe-0.1C-5Al based on the authors' previous report [19]. The properties assessed include the ultimate tensile strength (UTS, MPa), yield strength (YS, MPa), total elongation (%), Vickers hardness (HV), and toughness (J/m^2) at room temperature. The significant improvement in the mechanical properties observed for Fe-0.1C-5Al compared to Fe-0.1C-0.05Al, particularly the superior ductility and toughness despite the high strength due to the increased Al addition, indicates that the distinct mechanical behavior may arise from the thermomechanical effects of FSW not only on grain refinement but also on the changes in the carbide type and size. Compared to cementite, κ-carbides have a smaller average size under an equivalent thermodynamic effect [19]. This suggests that the deformation behavior of carbides during FSW plays a critical role in improving the mechanical properties. During the FSW process, mechanical stirring and thermal effects affect the state of the carbide. The mechanisms of carbide deformation are discussed in detail in Section 4.

3.3. Nano-hardness of cementite and κ-carbide

During the FSW process, cementite and κ-carbide underwent distinctively different deformation, primarily due to the intrinsic properties of the materials. Fig. 5a presents the nanoindentation profiles of cementite and κ-carbide precipitated in the SZs of Fe-0.1C-0.05Al and Fe-0.1C-5Al, respectively. The inset shows a SEM image of the test region, along with the indentations. Larger carbides were selected for testing, with a peak contact load of 800 μN, to minimize the indentation size effect (ISE) [36]. The nano-hardness was calculated using the Oliver and Pharr method [32]. The nano-hardness of cementite was approximately 13.0 GPa, whereas that of the κ-carbides was approximately 6.9 GPa. To quantify the deformation resistance due to cementite and κ-carbides, the relationship between P/h and h [37,38] was investigated (Fig. 5b), where P and h indicate the load and indentation depth,

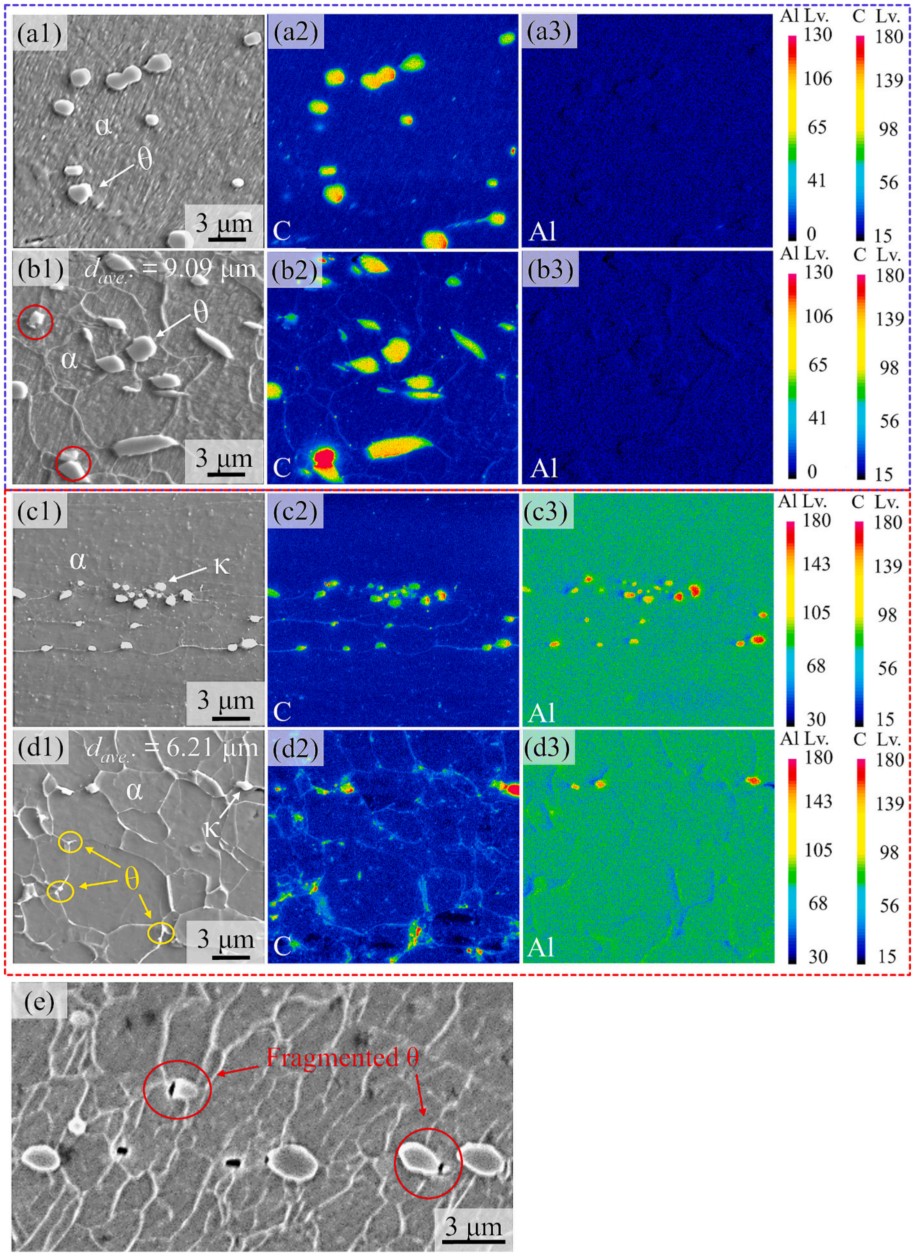

Fig. 3. SEM micrographs and WDS microanalysis elemental mappings of the corresponding regions by EPMA. (a1–a3) and (b1–b3) BM and SZ of Fe-0.1C-0.05Al. (c1–c3) and (d1–d3) BM and SZ of Fe-0.1C-5Al; (e) Supplementary figure showing partial fragmented cementite observed in the SZ of Fe-0.1C-5Al after FSW.

respectively. The slope of the curves, obtained through the least-squares approximation, can be evaluated as an index of the deformation resistance. The slope of the curve for cementite was approximately 0.22 μN/nm^2, which is significantly greater than the slope for the κ-carbide (0.083 μN/nm^2). This clear difference in the slope further underscores the higher deformation resistance of cementite compared to that of κ-carbide at room temperature. These analyses suggest that cementite is significantly harder and more brittle than κ-carbide. The difference in the deformation behaviors of these carbides during FSW is presumed to be closely linked to this finding, although there is a temperature difference. Notably, this study represents the first direct quantitative comparison of the hardness and deformation resistance of cementite and κ-carbides in the Fe-C-Al ternary system, moving beyond generalized or separate descriptions of the hardness and brittleness of these species [39,40].

3.4. *Thermal & mechanical dissolution of carbides during FSW*

Carbides may undergo thermal and mechanical dissolution when subjected to frictional heat and shear forces caused by the rotation and axial pressure of the stirring tool during the FSW process. As indicated by the phase diagrams in Fig. 6a,b, at 700 °C where FSW was conducted, the microstructures of Fe-0.1C-0.05Al and Fe-0.1C-5Al were characterized by ferrite + cementite + a small amount of solute carbon and ferrite + κ-carbide + a very small amount of solute carbon, respectively. Fig. 6c,d shows the isothermal ternary phase diagrams of Fe-0.1C-Al at 700 °C and 400 °C, respectively. As the temperature decreases, the C content in κ-carbides increases, indicating that κ-carbides are relatively stable and do not readily undergo thermal dissolution under the FSW conditions. Therefore, it was inferred that substantial thermal dissolution of carbides is unlikely during welding. Under FSW conditions below the A_1 temperature, accompanied by rapid cooling, the thermodynamic effects are minimal, making mechanical dissolution the dominant factor.

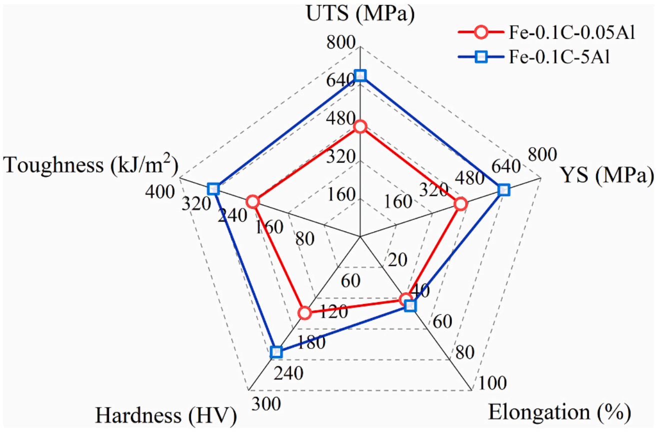

Fig. 4. Spider diagram of the mechanical properties of the SZs of Fe-0.1C-0.05Al and Fe-0.1C-5Al.

Previous studies have indicated that thin cementite in pearlite may decompose under severe plastic deformation when steel wires are drawn at room temperature. The primary mechanisms of cementite decomposition include (1) dislocation-C interactions during the plastic deformation of thin, lamellar cementite [21], where C atoms gain mobility due to the increased temperature during deformation and migrate toward high-density dislocation regions; (2) the Gibbs-Thomson effect [41], in which severe deformation fractures the cementite phase, increasing the interfacial free energy and enhancing the local solubility of C, thereby facilitating carbide decomposition; (3) the C-drag effect [42] where the strong affinity between C and dislocations leads to the transfer of C atoms from the carbides into ferrite as dislocations traverse the carbide/ferrite interface. Upon dislocation annihilation, the C atoms remain in the ferrite. These mechanisms can potentially explain the mechanical decomposition of carbides under severe plastic deformation. Accordingly, the deformation behavior and processes related to carbide decomposition during FSW were considered. During FSW, large elastic and plastic strains may occur within the carbides at elevated temperatures. However, owing to its hardness and brittleness, relatively coarse cementite presumably undergoes limited deformation compared to κ-carbides, reducing the likelihood of mechanical dissolution of the former [25].

The essential mechanical properties of crystalline materials, such as strength and ductility, are predominantly determined by the dislocation mobility and interactions between the dislocations and various microstructural features [43]. Typically, precipitates act as obstacles to dislocation gliding, and their interactions with dislocations contribute to material hardening [44]. The Orowan and cutting-through mechanisms are basic sources of metal strengthening by particles [45]. In the first scenario, at coherent or incoherent phase boundaries between the matrix and particles, which are sufficiently stronger than the matrix, the dislocation bypasses the particle owing to differences in the lattice structure, resulting in the formation of dislocation loops around the precipitate. In contrast, cutting-through (Friedel effect) occurs only at coherent or semicoherent phase boundaries, where the dislocation slip plane remains continuous on account of the compatibility of the lattice structures [46]. Notably, if the precipitated particles are hard, relatively large, and incoherent with the matrix, dislocations may struggle to bypass or cut through these obstacles, leading to their accumulation at the matrix-precipitate interface, potentially serving as nucleation sites for cracks. The accumulation of dislocations in front of obstacles creates stress concentrations, which are presumed to induce either fragmentation or mechanical dissolution of the particles, depending on their nature and size.

3.5. TEM analysis of cementite in the BM and SZ of Fe-0.1C-0.05 Al

Cementite exhibits high hardness, elasticity, and toughness [47]. Given its hardness, direct evidence of deformation is challenging to obtain, with crack rupture along certain fracture surfaces being one of the few visible indicators. Previous studies [48] on drawn pearlitic steel wires identified deformation traces of cementite along the drawing direction, but the information was limited to thin, lamellar pearlite and was ambiguous. To further elucidate the deformation behavior of relatively large cementite under FSW conditions below A_1, specimens from both the BM and SZ were prepared using FIB for TEM analysis. FIB milling was focused on the center of the selected cementite to ensure its inclusion in the upper section of the TEM specimen, where the thinner region near the ion beam source allowed for clearer observation of the internal microstructure of the carbide.

Fig. 7 illustrates the cementite located in the BM region of Fe-0.1C-0.05Al. The dark-field image (Fig. 7b1) obtained using a scanning transmission electron microscope (STEM) and the corresponding diffraction patterns obtained along the [0,1,0] zone axis (Fig. 7b2), along with energy-dispersive X-ray spectroscopy (EDS) analysis (Fig. 7c) confirmed that the carbides comprised orthorhombic-structured cementite. As indicated by the marked locations in Fig. 7a1,a2, a limited number of dislocations was clearly observed within the cementite. These dislocations were likely introduced during the multi-pass hot-rolling process at 700 °C, used to prepare the BM. Dislocations were also found at the interface between the cementite and ferrite, as well as in the region on the ferrite side at a small distance from the interface, as shown in Fig. 7a3. Although cementite is typically regarded as hard and brittle, the presence of these dislocations reveals that cementite presumably experiences stress or strain during hot rolling and plays a role in stress transfer and absorption during the overall plastic deformation, leading to subtle changes in its local microstructure.

The SZs of the FSW specimens are illustrated in Fig. 8, revealing three cementites approximately 2 μm in size, along the zone axis [2,2,1],

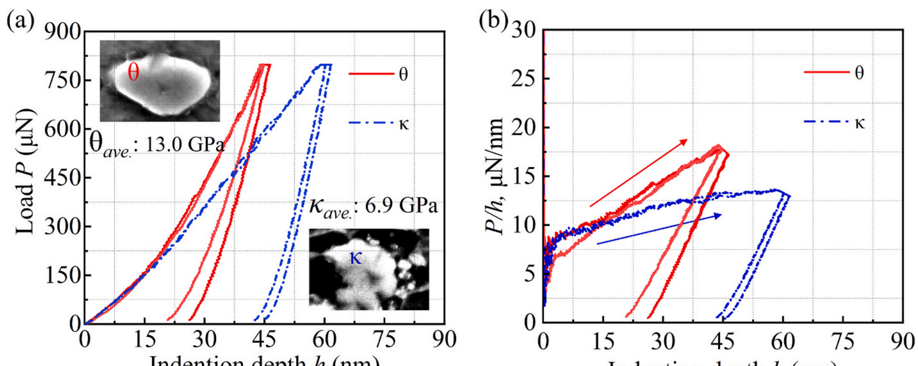

Fig. 5. (a) Nano-hardness load (*P*) vs. indentation depth (*h*) for areas of cementite and κ-carbide; (b) *P/h-h* curves of cementite and κ carbide.

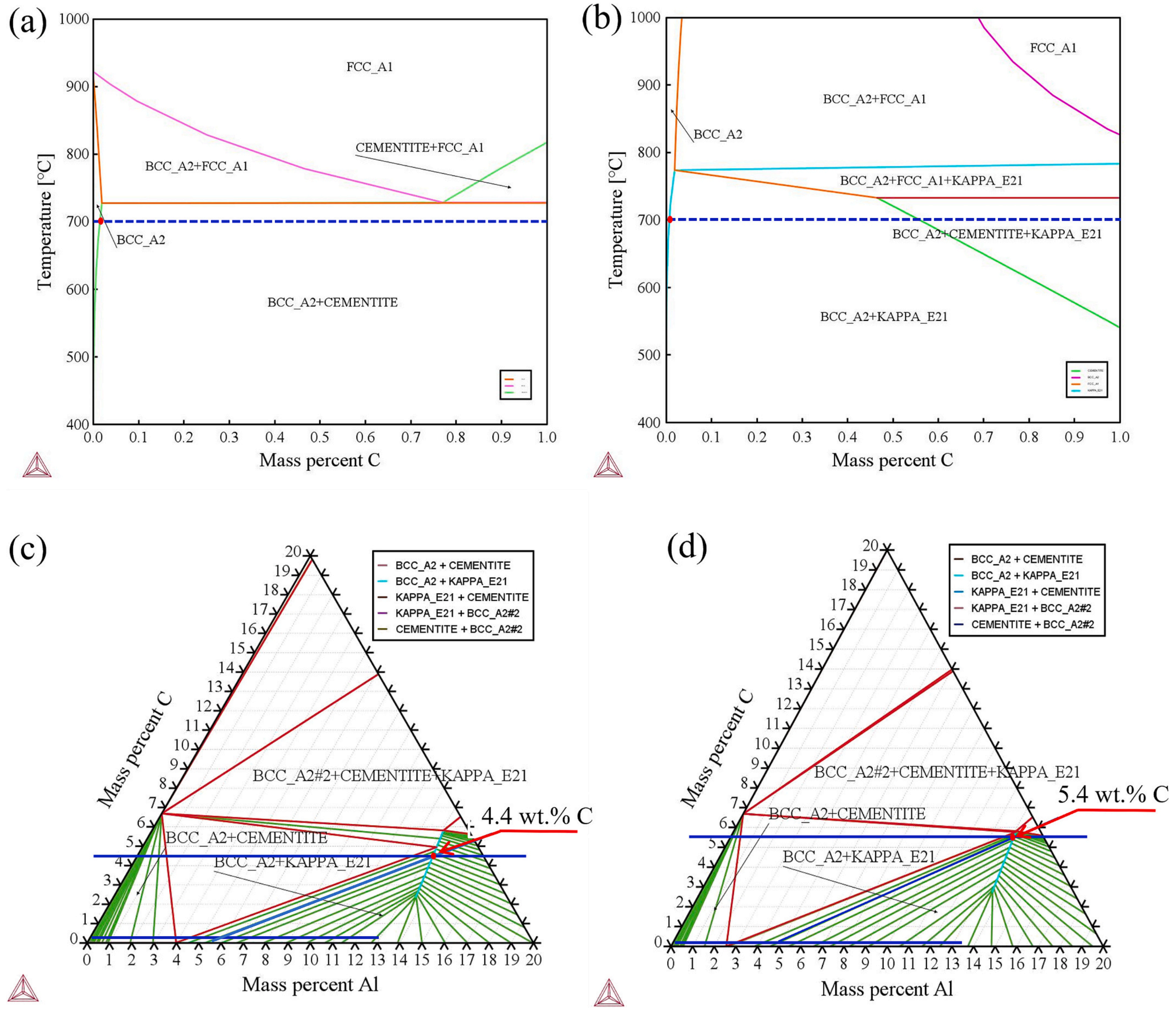

Fig. 6. Phase diagrams of (a) Fe-0.1C-0.05Al and (b) Fe-0.1C-5Al, isothermal section of Fe-0.1C-Al ternary phase diagrams at (c) 700 °C and (d) 400 °C, calculated with Thermo-Calc using TCFE9 database.

[1,1,4], and [1,0,1] (Fig. 8a1-c1). Fig. 8a1,b1 clearly shows the presence of dislocations within the cementite. Considering the dislocation morphology in the BM specimen, despite its hard and brittle nature, the cementite presumably experienced minor plastic deformation under the hot rolling and FSW conditions applied in this experiment. Furthermore, the dislocation density within the cementite of the BM and SZ specimens was not significantly different. The interface region between the cementite and ferrite was obviously different for the BM and SZ specimens. The number of dislocations at the ferrite-cementite interface in the BM (Fig. 7a3) was notably lower than that in the FSW specimen (Fig. 8b2), which suggests that the FSW process introduces and accumulates a significant number of dislocations in the ferrite region of the interface owing to the large plastic deformation introduced during the FSW process. The pronounced local strain gradient in the interface regions caused large deformation in the ferrite region, thereby introducing highly dense dislocations, which accumulated at the interface in the sustained state, as illustrated in Fig. 8b3. Therefore, dislocations primarily accumulated at the interface between cementite and ferrite under shear deformation. Consequently, the interaction between the cementite and dislocations under FSW conditions appears to align with the Orowan mechanism rather than with mechanisms such as the cut-through process. Increased stress concentration at the interface led to the fragmentation of a small portion of the cementite, even at elevated temperatures, although the experimental results show minor plastic deformation of cementite owing to the extremely limited deformability of the hard, brittle, and large cementite particles during the shear deformation process. This behavior contributes to the reduced ductility and toughness of engineering materials at room temperature [49].

Notably, the dislocation distribution in the two cementites differed: in Fig. 8a2, the dislocation lines are dispersed, whereas in Fig. 8b2, the dislocations are more concentrated. This discrepancy is likely attributable to the difference in the shear components around these precipitates during FSW. This observation was verified by the data in Fig. 8c1, where no dislocations were found within the cementite. Variations in the torsion angles and shear stress are presumed to produce different deformation behaviors. However, each observed dislocation within the cementite exhibited a slight curvature, whereas the overall extension of the cementite tended to follow a specific direction. It is speculated that

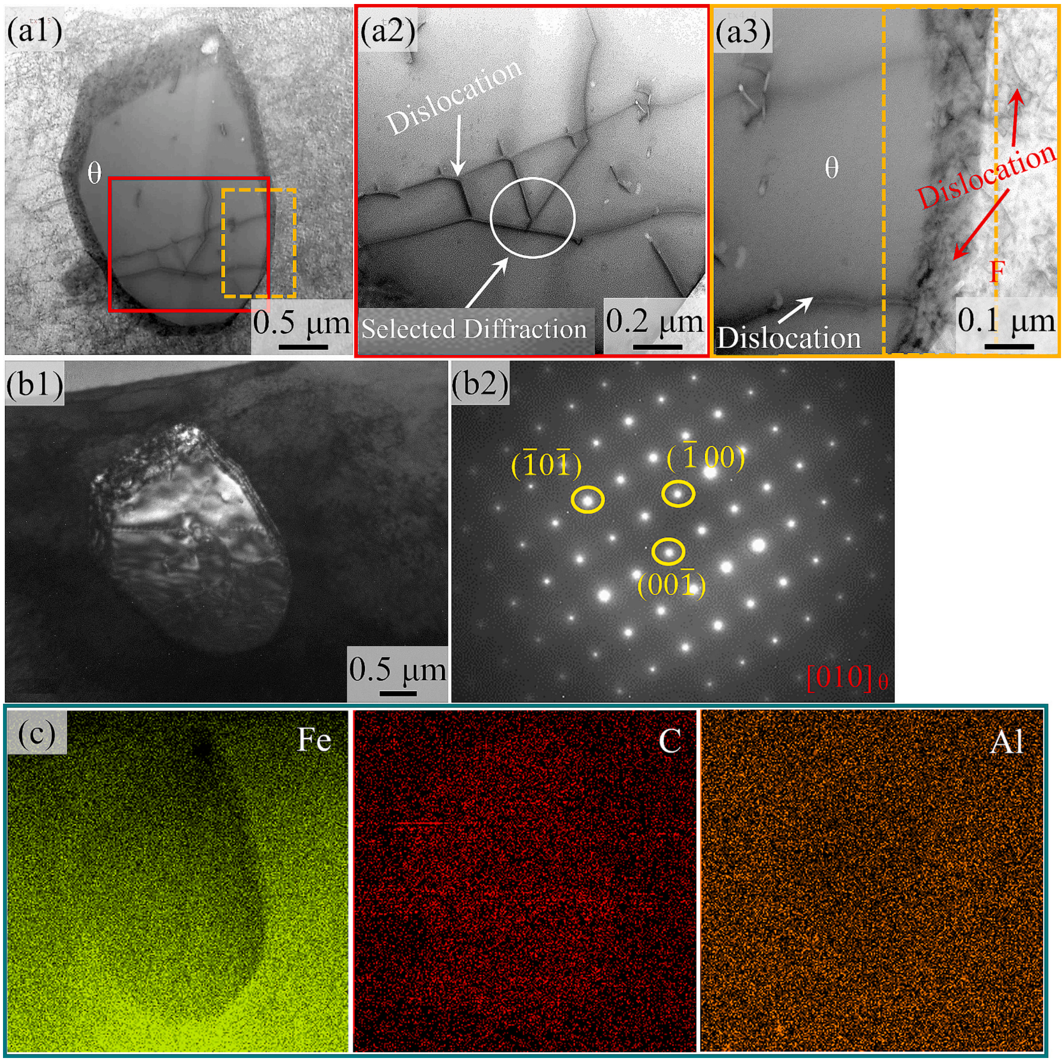

Fig. 7. TEM micrographs of FIB specimens from selected BM areas of Fe-0.1C-0.05Al; (a1) TEM bright-field image; (a2, a3) showing enlargement of the selected areas in (a1), respectively; (b1) TEM dark-field image; (b2) selected area electron diffraction; and (c) TEM EDS-mapping analysis of cementite.

only a single slip system is activated within cementite during shear deformation, making it difficult to activate multiple slip systems because of the hard and brittle nature of cementite. Furthermore, the relatively smooth surface of the cementite and minor reduction in its average size may be due to a certain degree of dynamic relaxation during the FSW process, which diminishes the effect of the stress concentration caused by dislocations and lowers the frequency of fractures. The deformation trajectory of the cementite appears to be associated with its (010) cleavage plane [50,51]. This aspect of the study will be addressed in future research.

3.6. TEM analysis of κ-carbide in the BM and SZ of Fe-0.1C-5 Al

Fig. 9 shows the carbide in the BM region of Fe-0.1C-5Al, which was confirmed to be κ-carbide with an $L1_2$-type crystal structure based on TEM-selected area electron diffraction along the $[1\bar{2}\bar{1}]$ zone axis (Fig. 9b3) and EDS elemental mapping (Fig. 9c). The internal dislocation in κ-carbide was visible, which was presumably introduced during hot rolling. Comparison of cementite in the BM of Fe-0.1C-0.05Al with κ-carbide in the BM of Fe-0.1C-5Al subjected to multi-pass hot rolling followed by isothermal annealing at 700 °C for 30 min showed only slight differences. Notably, some portions of the interface between the κ-carbides and the ferrite matrix presumably appeared to be semi-coherent. The presence of semicoherent interfaces can be inferred from the Moiré fringes or other interference patterns resulting from crystal misorientation (as shown in Fig. 9a3), along with the significant number of dislocations observed at the boundary at different crystal tilt angles (Fig. 9b1). This misfit primarily arises from the differences in the lattice parameters, leading to increased stress near the interface. Under such conditions, the boundaries between the matrix and precipitate may gradually transition into coherent or semicoherent interfaces. Although coherent interfaces generally imply good lattice matching, semicoherent interfaces typically incorporate dislocations to manage partial lattice misfits [46]. In semicoherent interfaces, a partial lattice misfit typically results in the generation of dislocations to accommodate mismatched regions, thereby allowing the two adjacent crystal structures or orientations to adjust and alleviate the strain induced by the lattice mismatch at the boundary. In regions subjected to high strain or significant plastic deformation [52], the interface between the κ-carbides and the ferrite matrix exhibits substantial elastic strain, causing local disorder in the crystal structure and misorientation. Note that the presence of such semicoherent interfaces is presumed to allow shearing of the κ-carbide during interactions with dislocations under conditions of large plastic deformation.

For the SZ specimens of Fe-0.1C-5Al, distinctly different carbide deformation behavior was interestingly observed. Fig. 10 shows the three κ-carbides at the selected locations, which were densely filled with dislocation lines that were notably bent and disordered. Owing to their

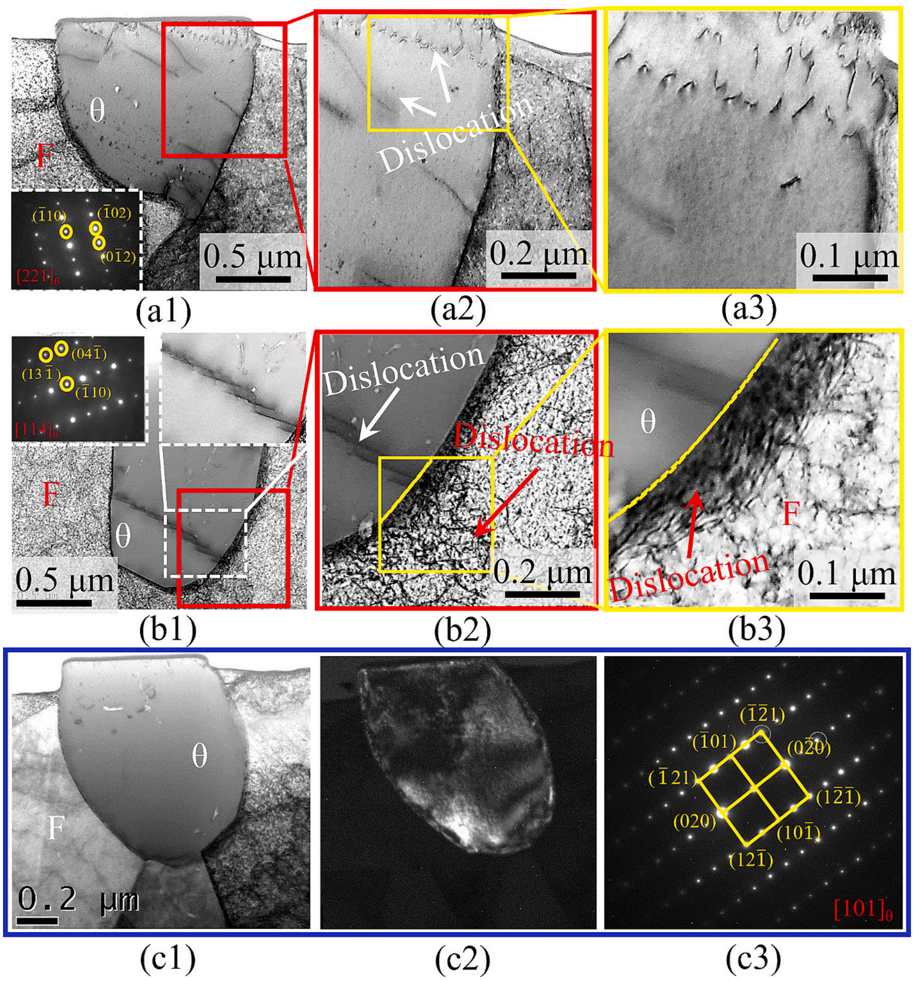

Fig. 8. TEM micrographs of FIB specimens from selected SZ areas of Fe-0.1C-0.05Al, including three carbides; (a1, b1) TEM bright-field image with selected area electron diffraction of cementite; (a2, b2) enlargement of the selected area in (a1) and b1, respectively; (a3, b3) enlargement of the selected area in (a2) and (b2), respectively; (c1) TEM bright-field image, (c2) TEM dark-field image, and (c3) electron diffraction of a selected area of dislocation-free cementite.

relatively softer nature compared to cementite, it is speculated that multiple slip systems were activated within the κ-carbides under shear deformation, and the κ-carbides experienced significant plastic deformation during the FSW process. The κ-carbides introduced numerous internal dislocations, which are presumably coordinated with dislocations located at the neighboring ferrite boundary [53], and the dislocations are presumed to cut through the κ-carbides [22,54]. This process is aligned with the cut-through mechanism [46]. Under shear stress, the deformability of ferrite facilitates the introduction of numerous dislocations, while the relatively soft nature of κ-carbide is assumed to simultaneously lead to the generation of internal dislocations. The semicoherent phase boundaries presumably enable the dislocation slip to overcome the resistance posed by the κ-carbides, thereby inducing shearing. The enlarged view of the dashed box in Fig. 10II reveals that less dislocation density accumulated at the ferrite/κ-carbide interface because the existing κ-carbides allow dislocation shearing.

The strong attractive interaction energy (0.8 eV/atom) between the high-density mobile dislocations and C atoms exceeds the bonding energy between Fe and C in cementite (0.5 eV/atom) and the κ-carbides (0.29 eV/atom) [21,55]. Notably, the bonding energy between Fe and C in κ-carbide is much smaller than that in cementite; thus, dislocations can trap C atoms in κ-carbide and transfer them to the α-ferrite matrix. This novel process is attributed to the localized stress fields generated by the dislocations, which attract and trap C atoms, outweighing the bonding energies within the carbides. Some of the C atoms captured in the dislocations diffused toward the grain boundaries with a deeper attractive potential. Moreover, as the dislocations intersected and formed pairs, leading to partial annihilation and rearrangement at elevated temperatures, the released C atoms diffused toward parts of the grain boundaries, and the segregated C led to the precipitation of fine cementite particles at the grain boundaries. This inference corresponds to the observed precipitation of fine cementite in the SZ of Fe-0.1C-5Al. The motion of the high-density dislocations that "capture" C atoms is analogous to the tendency of solute atoms (such as C and N) to segregate at defects (e.g., dislocations, interfaces) to minimize the free energy in the system [56,57].

3.7. Formation of intergranular cementite during cooling after FSW of Fe-0.1C-5Al

To quantitatively determine whether the inferences made in the previous section regarding the precipitation behavior of fine cementite at the grain boundaries in the SZ of the Fe-0.1C-5Al specimen are valid, the diffusion distance of C atoms in ferrite during the cooling phase after FSW was evaluated (using the diffusion distance of Al as a reference). Fig. 11 shows the heat cycle measurements obtained using a thermocouple during FSW under the same welding conditions.

The lattice diffusion coefficient D is commonly utilized to assess the diffusion distance, L, of a solute and is calculated using Eqs. (1) and (2).

$$D = D_0 exp\left(-\frac{Q}{RT}\right) \tag{1}$$

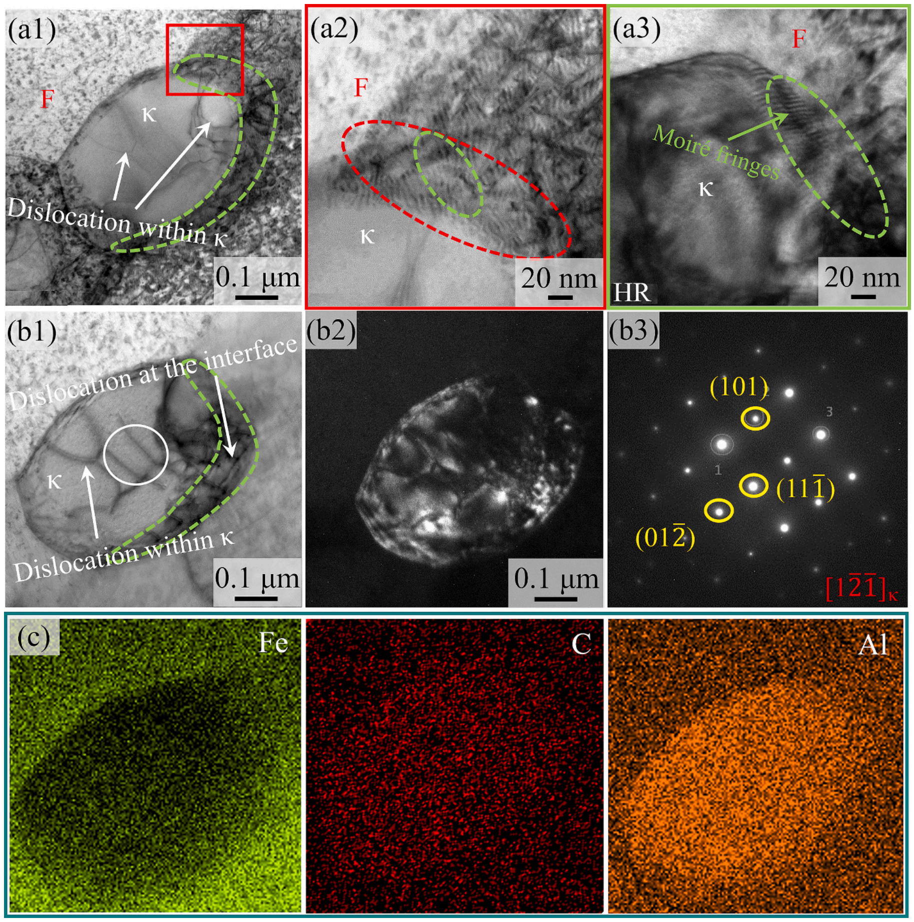

Fig. 9. TEM micrographs of FIB specimens from selected BM areas of Fe-0.1C-5Al; (a1) bright-field image; (a2, a3) enlargement of selected areas in (a1), respectively; (b1) TEM bright-field image at different tilt stage angles; (b2) TEM dark-field image; (b3) selected area electron diffraction; (c) TEM EDS-mapping analysis of κ carbide.

The pre-exponential factor and activation energy for C diffusion in ferrite are $D_0 = 2 \times 10^{-6}$ m^2/s [59] and $Q = 87.4$ kJ/mol [60], and those for Al diffusion in ferrite are $D_0 = 2.4 \times 10^{-16}$ m^2/s [61] and $Q = 142$ kJ/mol [62], respectively; R is the gas constant (8.314 J/mol·K). Given that the diffusion rate of C atoms decreases significantly below 200 °C, C diffusion is considered negligible at lower temperatures [63]. During this period of several seconds, C atoms complete the main diffusion process and accumulate at the grain boundaries. The diffusion distance, L, is expressed as:

$$L^2 = \int_{t_0}^{t_f} D\mathrm{d}t = D_0 \int_{t_0}^{t_f} exp\left(-\frac{Q}{RT(t)}\right)\mathrm{d}t \tag{2}$$

where t_0 and t_f are the time at the start and finish (200 °C) of cooling (see Fig. 11). The diffusion distance of the C and Al atoms during the FSW was estimated to be approximately 45 μm and 4.2×10^{-6} μm, respectively, which, in the case of C, significantly exceeds the radius of the ferrite grains (~3 μm) in the SZ of FSW below A_1. Grain boundary precipitation of fine cementite is inferred to take place during the cooling phase of FSW.

3.8. Verification of dissolution and reprecipitation behavior of carbides during FSW

To further verify the hypothesis that the partial dissolution of κ-carbides is followed by the precipitation of fine cementite at the grain boundaries in the SZ during FSW, post heat-treatment was performed at 700 °C for 10 min. Under the set conditions, the metastable fine cementite in the SZ of Fe-0.1C-5Al is expected to dissolve first [64], after which the stable κ-carbides precipitate.

In Fe-0.1C-0.05Al, cementites persisted in the SZ after the post-heat treatment, as shown in Fig. 12a,b1. The carbide type was determined through selected-area electron diffraction (Fig. 12b3) and EDS analysis (Fig. 12c). Even after the post-heat treatment, dislocations were still observed within the cementite, as shown in Fig. 12b2. In contrast, it is interesting that a significant amount of carbides precipitated in the SZ of Fe-0.1C-5Al after the post heat-treatment, all of which were identified as κ-carbide through TEM and EDS analyses, with no detection of cementite. This suggests that the fine cementite at the grain boundaries in the SZ first dissolved and were then transformed into κ-carbide. Consequently, the hypothesis that κ-carbide dissolves, accompanied by the formation of metastable cementite during FSW of Fe-0.1C-5Al was verified.

Statistical analysis of the changes in the type, size, and number of carbides during FSW and post-heat treatment was conducted for the Fe-0.1C-0.05Al and Fe-0.1C-5Al specimens. In Fe-0.1C-0.05Al, the cementite particles with a size of approximately 1.7 μm experience minor plastic deformation under the shear forces during the FSW process. Given their inherent hardness and brittleness, these cementites are prone to fragmentation under stress, resulting in an average size reduction to approximately 1.2 μm (Fig. 13b). Following the post heat-treatment, the cementites grew slightly to a size of ca. 1.4 μm, with no other carbide type detected (Fig. 13c). Furthermore, during this post-annealing stage, an overall slight coarsening of the particles, regardless of the type of carbide, occurred through Ostwald ripening [65], which is commonly used to explain the morphological changes that

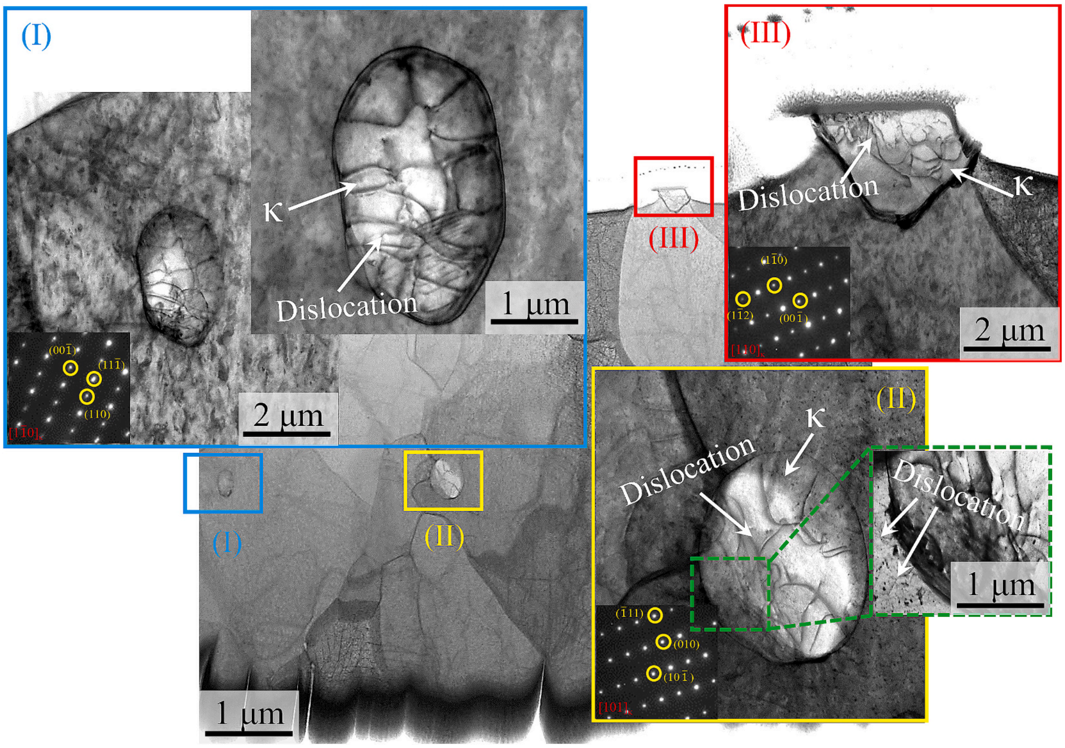

Fig. 10. TEM micrographs of FIB specimens from selected SZ areas of Fe-0.1C-5Al, including three carbides (I, II, III) with corresponding magnified images and electron diffraction of the selected area.

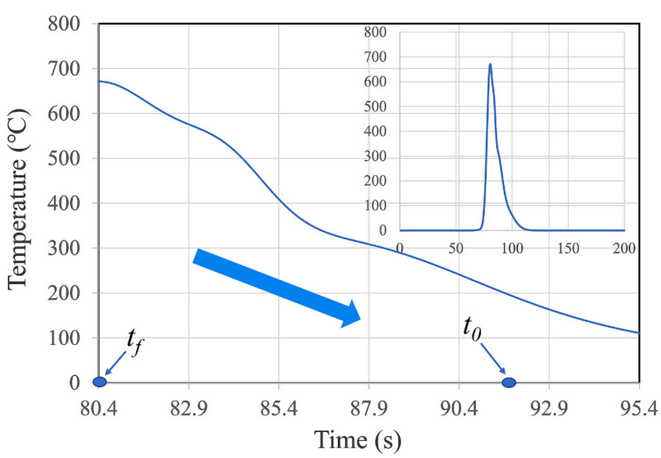

Fig. 11. Heat cycle during FSW, measured using thermocouples [58].

occur at the end of a first-order transformation driven by a reduction in the interfacial energy. Decreasing the total interfacial energy increases the size of the coarsened particles through diffusive mass flow from the shrinking to growing precipitates at the expense of the smaller ones [66]. In other words, the thermal effect of post heat-treatment, i.e., holding at 700 °C for 10 min, causes coarsening of the cementite in the SZ of Fe-0.1C-0.05Al. On the other hand, after FSW, smaller particles of residual κ-carbides were observed in the SZ of Fe-0.1C-5Al, along with fine intergranular cementite. Post heat-treatment initially led to the dissolution of fine cementite, with subsequent precipitation of a significant number of stable κ-carbides (0.2 μm) at the grain boundaries (Fig. 13d,e1,e2,f). Elemental analysis of the carbides precipitated at the grain boundaries in the statistical region revealed that all the carbides were κ-carbides, with no evidence of cementite. The thermal effect of post heat-treatment causes the small cementite particles to dissolve and reprecipitate as small κ-carbides, accompanied by growth of the remaining κ-carbides in the SZ of Fe-0.1C-5Al.

3.9. Proposed mechanisms of cementite and κ-carbide deformation during FSW

Fig. 14 presents a schematic of the evolution of cementite and κ-carbides in the SZ of Fe-0.1C-0.05Al and Fe-0.1C-5Al during FSW below the A_1 temperature. The FSW process is divided into three stages. The cementite in Fe-0.1C-0.05Al undergoes slight plastic deformation under the influence of shear forces, and the strain distribution introduces numerous dislocations at the cementite/ferrite interface. As the dislocations accumulate, their large size and the hard and brittle nature of cementite make it difficult for dislocations to cut through the cementite, leading to stress concentration at the interface and partial fragmentation of cementite, presumably due to dynamic relaxation of the concentrated stress at the interface. In contrast, the softer κ-carbide in Fe-0.1C-5Al forms dislocations, resulting from significant plastic deformation and the low density of dislocations at the κ-carbide/ferrite interface, caused by the ability of the dislocations to cut through the κ-carbides, facilitated by the semicoherent interface. This process ultimately resulted in the observed smaller size of the remaining κ-carbide. Meanwhile, the C atoms from the κ-carbide are captured by dislocations and transferred into the ferrite region. As the dislocations merge and are annihilated at elevated temperatures, these unbound C atoms diffuse and segregate at the grain boundaries, leading to the formation of very fine, semi-stable cementite in a network or semi-network structure during FSW.

4. Conclusions

The novel deformation behavior of cementite and κ-carbide during FSW of Fe-0.1C-0.05Al and Fe-0.1C-5Al (mass%) steels below the A_1 temperature was systematically evaluated by clarifying the internal dislocation characteristics of the deformed carbides. The results are as

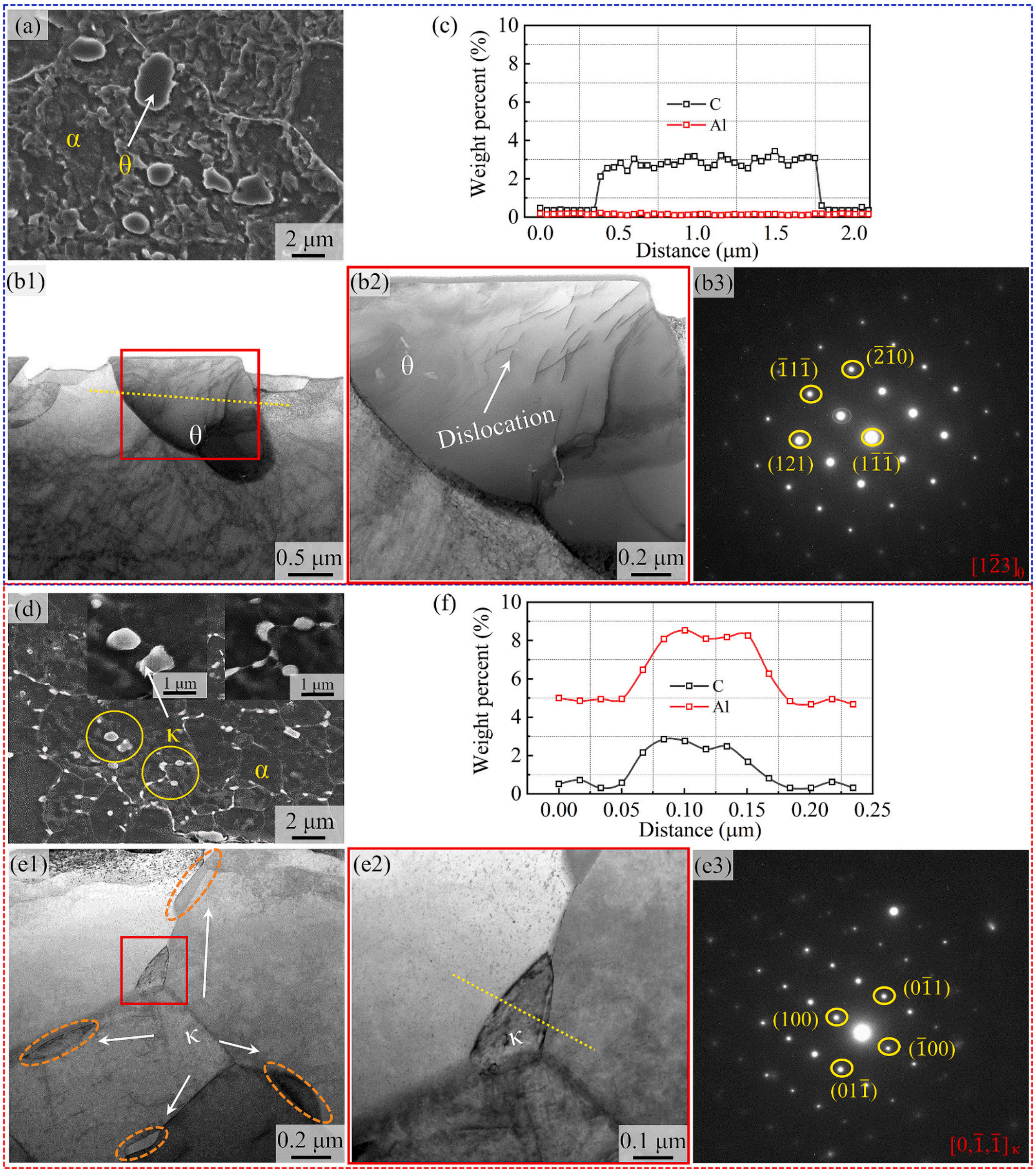

Fig. 12. (a) SEM image of SZ after post heat-treatment of Fe-0.1C-0.05Al at 700 °C for 10 min; (b1) TEM bright-field image of cementite with corresponding (b2) magnified images and (b3) selected area electron diffraction of cementite; (c) TEM EDS-line analysis of cementite; (d) SEM image of SZ after post heat-treatment of Fe-0.1C-5Al at 700 °C for 10 min; (e1) TEM bright-field image of κ-carbide with corresponding (e2) magnified images and (e3) selected area electron diffraction pattern of κ-carbide; (f) TEM EDS-line analysis of κ-carbide.

follows:

(1) Nano-indentation tests revealed for the first time that the nanohardness of cementite (13.0 GPa) was greater than that of the κ-carbides (6.9 GPa). During FSW, the cementite undergoes slight plastic deformation, followed by rupture, due to its hard and brittle nature, while the κ-carbide experiences significant plastic deformation.
(2) In the SZ of the Fe-0.1C-0.05Al joint, shear forces introduced a large number of dislocations at the interface between the cementite and ferrite matrix. The accumulation of these dislocations, combined with the brittle and hard nature of cementite, prevents dislocation bypasses or penetration, resulting in local stress concentration and eventual fragmentation of cementite.
(3) In contrast, in the SZ of the Fe-0.1C-5Al joint, the relative softness of κ-carbide allows dislocations that accumulate at the interface to cut through the interface. The moving dislocations capture C atoms and transfer them into the ferrite region; namely, mechanical dissolution occurs where C atoms diffuse to the grain boundaries, leading to the precipitation of fine cementite during FSW.

CRediT authorship contribution statement

Junqi Chen: Writing – original draft, Validation, Software, Methodology, Investigation, Formal analysis, Data curation, Conceptualization. **Takuya Miura:** Investigation, Writing – review & editing, Funding acquisition, Supervision. **Kohsaku Ushioda:** Writing – review & editing, Visualization, Supervision, Conceptualization. **Hidetoshi Fujii:** Writing – review & editing, Supervision, Project administration, Funding acquisition, Conceptualization.

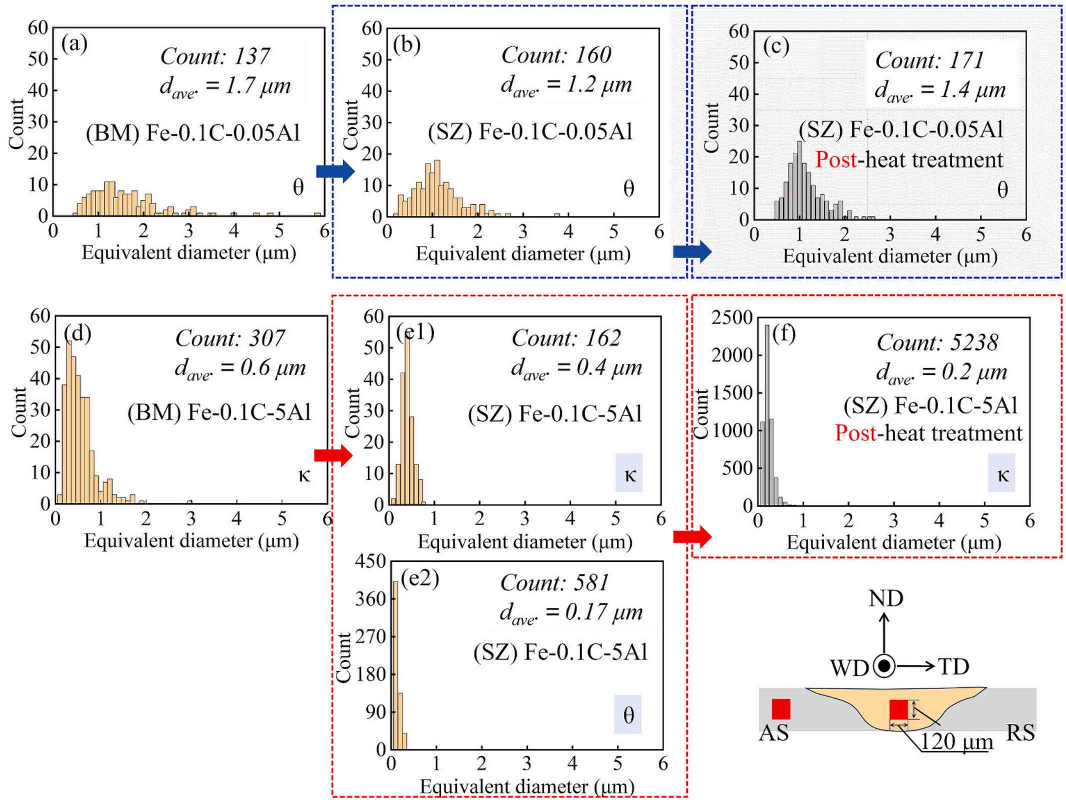

Fig. 13. Statistics of carbide type, dimensions, and number in BM, SZ, and post heat-treated specimens of (a–c) Fe-0.1C-0.05Al and (d–f) Fe-0.1C-5Al.

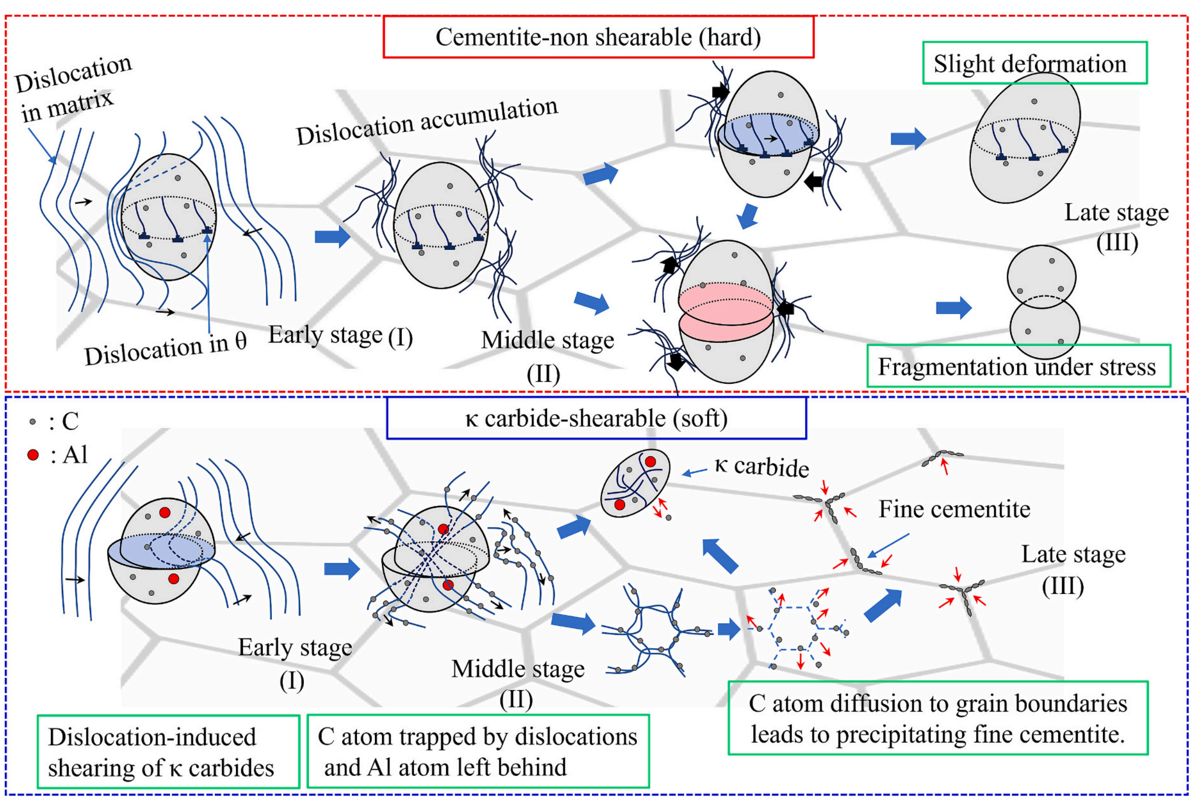

Fig. 14. Schematic of the deformation of cementite and κ-carbide during FSW.

Declaration of competing interest

The authors declare that they have no competing financial interests or personal relationships that may have influenced the work reported in this study.

Acknowledgments

This work was supported by the JST-Mirai Program (grant number JPMJMI19E5) and JSPS KAKENHI (grant numbers JP19H00826 and JP23K13576). The authors appreciate the financial support provided by the ISIJ Research Project of the Iron and Steel Institute of Japan.

Data availability

The raw/processed data required to reproduce these findings cannot be shared at this time, as the data also form part of an ongoing study.

References

[1] R.G. Baligidad, U. Prakash, A.R. Krishna, Thermal stability and elevated temperature mechanical properties of electroslag remelted Fe-16wt.%Al-(0.14-0.5) wt.% C intermetallic alloys, Mater. Sci. Eng. A 230 (1997) 188–193, https://doi.org/10.1016/S0921-5093(97)00031-2.

[2] V.V. Satya Prasad, S. Khaple, R.G. Baligidad, Melting, processing, and properties of disordered Fe-Al and Fe-Al-C based alloys, JOM 66 (2014) 1785–1793, https://doi.org/10.1007/s11837-014-1065-1.

[3] S. Khaple, B.R. Golla, V.V.S. Prasad, A review on the current status of Fe-Al based ferritic lightweight steel, Def. Technol. 26 (2023) 1–22, https://doi.org/10.1016/j.dt.2022.11.019.

[4] J.A. Jiménez, G. Frommeyer, The ternary iron aluminum carbides, J. Alloys Compd. 509 (2011) 2729–2733, https://doi.org/10.1016/j.jallcom.2010.12.017.

[5] G. Frommeyer, U. Brüx, Microstructures and mechanical properties of high-strength Fe-Mn-Al-C light-weight TRIPLEX steels, Steel Res. Int. 77 (2006) 627–633, https://doi.org/10.1002/srin.200606440.

[6] S. Jeong, G. Park, B. Kim, J. Moon, S.J. Park, C. Lee, Precipitation behavior and its effect on mechanical properties in weld heat-affected zone in age hardened FeMnAlC lightweight steels, Mater. Sci. Eng. A 742 (2019) 61–68, https://doi.org/10.1016/j.msea.2018.10.125.

[7] T. Doi, K. Kitamura, K. Nakanishi, K. Kashima, T. Kamimura, H. Miyuki, T. Ohta, M. Yamashita, Characterization of rust layers formed on Al bearing steels exposed to coastal environments, J. Jpn. Inst. Metals 74 (2010) 10–18, https://doi.org/10.2320/jinstmet.74.10.

[8] J. Herrmann, G. Inden, G. Sauthoff, Deformation behaviour of iron-rich iron-aluminum alloys at low temperatures, Acta Mater. 51 (2003) 2847–2857, https://doi.org/10.1016/S1359-6454(03)00089-2.

[9] G. Frommeyer, E.J. Drewes, B. Engl, Physical and mechanical properties of iron-aluminium-(Mn, Si) lightweight steels, Metall. Res. Technol. 97 (2000) 1245–1253, https://doi.org/10.1051/metal:2000110.

[10] K.W. Andrews, The structure of cementite and its relation to ferrite, Acta Metall. 11 (1963) 939–946, https://doi.org/10.1016/0001-6160(63)90063-4.

[11] E.P. Elsukov, G.A. Orofeev, A.L. Yanov, D.A. Vytovtov, On the problem of the cementite structure, Phys. Met. Metallogr. 102 (2006) 76–82, https://doi.org/10.1134/S0031918X06070106.

[12] S.S. Sohn, B.J. Lee, S. Lee, N.J. Kim, J.H. Kwak, Effect of annealing temperature on microstructural modification and tensile properties in 0.35 C–3.5 Mn–5.8 Al lightweight steel, Acta Mater. 61 (2013) 5050–5066, https://doi.org/10.1016/j.actamat.2013.04.038.

[13] J.C. Pang, W.F. Yang, G.D. Wang, S.J. Zheng, R.D.K. Misra, H.L. Yi, Divorced eutectoid transformation in high-Al added steels due to heterogenous nucleation of κ-carbide, Scr. Mater. 209 (2022) 114395, https://doi.org/10.1016/j.scriptamat.2021.114395.

[14] R.G. Baligidad, K.S. Prasad, Effect of Al and C on structure and mechanical properties of Fe–Al–C alloys, Mater. Sci. Technol. 23 (2007) 38–44, https://doi.org/10.1179/174328407X158389.

[15] S. Chen, R. Rana, A. Haldar, Current state of Fe-Mn-Al-C low density steels, Prog. Mater. Sci. 89 (2017) 345–391, https://doi.org/10.1016/j.pmatsci.2017.05.002.

[16] H.L. Yi, H.L. Cai, Z.Y. Hou, J.C. Pang, D. Wu, G.D. Wang, Low density steel 1·2C–1·5Cr–5Al designed for bearings, Mater. Sci. Technol. 30 (2014) 1045–1049, https://doi.org/10.1179/1743284714Y.0000000513.

[17] N. Yoshimura, K. Ushioda, M. Yonemura, M. Koyama, M. Tanaka, H. Noguchi, Effect of the state of carbon on ductility in Fe-0.017mass%C ferritic steel, Mater. Sci. Eng. A 701 (2017) 120–128, https://doi.org/10.1016/j.msea.2017.06.070.

[18] N.J. Petch, The influence of grain boundary carbide and grain size on the cleavage strength and impact transition temperature of steel, Acta Metall. 34 (1986) 1387, https://doi.org/10.1016/0001-6160(86)90026-X.

[19] J. Chen, T. Miura, K. Ushioda, H. Fujii, Microstructures and mechanical properties of FSWed Fe-xAl and Fe-0.1C-xAl alloys, J. Mater. Res. Technol. 36 (2025) 888–902, https://doi.org/10.1016/j.jmrt.2025.03.140.

[20] Y. Li, D. Raabe, M. Herbig, P.P. Choi, S. Goto, A. Kostka, H. Yarita, C. Borchers, R. Kirchheim, Segregation stabilizes nanocrystalline bulk steel with near theoretical strength, Phys. Rev. Lett. 113 (2014) 106104, https://doi.org/10.1103/PhysRevLett.113.106104.

[21] X. Sauvage, Y. Ivanisenko, The role of carbon segregation on nanocrystallisation of pearlitic steels processed by severe plastic deformation, J. Mater. Sci. 42 (2007) 1615, https://doi.org/10.1007/s10853-006-0750-z.

[22] M.J. Yao, E. Welsch, D. Ponge, S.M.H. Haghighat, S. Sandlöbes, P. Choi, M. Herbig, I. Bleskov, T. Hickel, M. Lipinska-Chwalek, P. Shanthraj, C. Scheu, S. Zaefferer, B. Gault, D. Raabe, Strengthening and strain hardening mechanisms in a precipitation-hardened high-Mn lightweight steel, Acta Mater. 140 (2017) 258–273, https://doi.org/10.1016/j.actamat.2017.08.049.

[23] R.G. Baligidad, A. Radhakrishna, Effect of hot rolling and heat treatment on structure and properties of high carbon Fe–Al alloys, Mater. Sci. Eng. A 308 (2001) 136–142, https://doi.org/10.1016/S0921-5093(00)02026-8.

[24] H. Ishii, K. Ohkubo, S. Miura, T. Mohri, Mechanical properties of α+κ two-phase lamellar structure in Fe–Mn–Al–C alloy, Mater. Trans. 44 (2003) 1679–1681, https://doi.org/10.2320/matertrans.44.1679.

[25] A. Taniyama, T. Takayama, M. Arai, T. Hamada, Deformation behavior of cementite in deformed high carbon steel observed by X-ray diffraction with synchrotron radiation, Metall. Mater. Trans. A 48 (2017) 4821–4830, https://doi.org/10.1007/s11661-017-4229-0.

[26] H. Fujii, L. Cui, N. Tsuji, M. Maeda, K. Nakata, K. Nogi, Friction stir welding of carbon steels, Mater. Sci. Eng. A 429 (2006) 50–57, https://doi.org/10.1016/j.msea.2006.04.118.

[27] Q. Wei, L. Kecskes, T. Jiao, K.T. Hartwig, K.T. Ramesh, E. Ma, Adiabatic shear banding in ultrafine-grained Fe processed by severe plastic deformation, Acta Mater. 52 (2004) 1859–1869, https://doi.org/10.1016/j.actamat.2003.12.025.

[28] R.Z. Valiev, R.K. Islamgaliev, I.V. Alexandrov, Bulk nanostructured materials from severe plastic deformation, Prog. Mater. Sci. 45 (2000) 103–189, https://doi.org/10.1016/S0079-6425(99)00007-9.

[29] N. Tsuji, Y. Saito, H. Utsunomiya, S. Tanigawa, Ultra-fine grained bulk steel produced by accumulative roll-bonding (ARB) process, Scr. Mater. 40 (1999) 795–800, https://doi.org/10.1016/S1359-6462(99)00015-9.

[30] J. Yoo, B. Kim, Y. Park, C. Lee, Microstructural evolution and solidification cracking susceptibility of Fe-18Mn-0.6C-xAl steel welds, J. Mater. Sci. 50 (2015) 279–286, https://doi.org/10.1007/s10853-014-8586-4.

[31] L. Cui, H. Fujii, N. Tsuji, K. Nakata, K. Nogi, R. Ikeda, M. Matsushita, Transformation in stir zone of friction stir welded carbon steels with different carbon contents, ISIJ Int. 47 (2007) 299–306, https://doi.org/10.2355/isijinternational.47.299.

[32] W.C. Oliver, G.M. Pharr, An improved technique for determining hardness and elastic modulus using load and displacement sensing indentation experiments, J. Mater. Res. 7 (1992) 1564–1583, https://doi.org/10.1557/JMR.1992.1564.

[33] M. Palm, G. Inden, Experimental determination of phase equilibria in the Fe-Al-C system, Intermetallics 3 (1995) 443–454, https://doi.org/10.1016/0966-9795(95)00003-H.

[34] H.N. Choi, J.W. Choi, H. Kang, H. Fujii, S.J. Lee, Effect of stacking-fault energy on dynamic recrystallization, textural evolution, and strengthening mechanism of Fe−Mn based twinning-induced plasticity (TWIP) steels during friction-stir welding, J. Adv. Join. Process. 10 (2024) 100236, https://doi.org/10.1016/j.jajp.2024.100236.

[35] J. Chen, T. Miura, K. Ushioda, H. Fujii, Effects of microstructure and phosphorus segregation on tensile properties of friction stir welded high phosphorus weathering steel, Mater. Sci. Eng. A 916 (2024) 147315, https://doi.org/10.1016/j.msea.2024.147315.

[36] Yu.V. Milman, A.A. Golubenko, S.N. Dub, Indentation size effect in nanohardness, Acta Mater. 59 (2011) 7480–7487, https://doi.org/10.1016/j.actamat.2011.08.027.

[37] K. Sekido, T. Ohmura, T. Sawaguchi, M. Koyama, H.W. Park, K. Tsuzaki, Nanoindentation/atomic force microscopy analyses of ε-martensitic transformation and shape memory effect in Fe–28Mn–6Si–5Cr alloy, Scr. Mater. 65 (2011) 942–945, https://doi.org/10.1016/j.scriptamat.2011.08.010.

[38] K. Nakano, K. Takeda, S. Ii, T. Ohmura, Evaluation of grain boundary strength through nanoindentation technique, J. Jpn. Inst. Met. Mater. 85 (2021) 40–48, https://doi.org/10.2320/jinstmet.jd202006.

[39] M. Umemoto, H. Ohtsuka, Mechanical properties of cementite, ISIJ Int. 62 (2022) 1313–1333, https://doi.org/10.2355/isijinternational.ISIJINT-2022-048.

[40] B.S. Lou, Y.Y. Chen, Z.Y. Wu, Y.C. Kuo, J.G. Duh, J.W. Lee, (Fe,Mn)3AlCx κ-carbide formation and characterization in pack aluminization of Fe–29Mn–9Al–0.9C lightweight steel, J. Mater. Res. Technol. 20 (2022) 1524–1532, https://doi.org/10.1016/j.jmrt.2022.07.179.

[41] Y. Daitoh, T. Hmada, Microstructures of heavily-deformed high carbon steel wires, Tetsu-to-Hagane 86 (2000) 105–110, https://doi.org/10.2355/tetsutohagane1955.86.2_105.

[42] A.V. Korznikov, Y.V. Ivanisenko, D.V. Laptionok, Influence of severe plastic deformation on structure and phase composition of carbon steel, Nanostruct. Mater. 4 (1994) 159–167, https://doi.org/10.1016/0965-9773(94)90075-2.

[43] P.M. Anderson, J.P. Hirth, J. Lothe, Theory of Dislocations, Cambridge University Press, United Kingdom, 2017.

[44] A.J. Ardell, Precipitation hardening, Metall. Trans. A. 16 (1985) 2131–2165, https://doi.org/10.1007/BF02670416.

[45] T. Gladman, Precipitation hardening in metals, Mater. Sci. Technol. 15 (1999) 30–36, https://doi.org/10.1179/026708399773002782.

[46] J.K. Lopez Barrilao, T. Beck, L. Singheiser, Microstructure Evolution of Laves Phase Strengthened Ferritic Steels for High Temperature Applications, Lehrstuhl für

Werkstoffe der Energietechnik (FZ Jülich), 2017, https://doi.org/10.18154/RWTH-2017-01982. Ph.D. Thesis.
[47] H.K.D.H. Bhadeshia, Cementite, IMR 65 (2020) 1–27, https://doi.org/10.1080/09506608.2018.1560984.
[48] J.D. Embury, R.M. Fisher, The structure and properties of drawn pearlite, Acta Metall. 14 (1966) 147–159, https://doi.org/10.1016/0001-6160(66)90296-3.
[49] K. Lu, The future of metals, Science 328 (2010) 319–320, https://doi.org/10.1126/science.1185866.
[50] K. Shibanuma, S. Aihara, S. Ohtsuka, Observation and quantification of crack nucleation in ferrite-cementite steel, ISIJ Int. 54 (2014) 1719–1728, https://doi.org/10.2355/isijinternational.54.1719.
[51] N. Yoshimura, K. Ushioda, H. Shirahata, M. Hoshino, G. Shigesato, M. Tanaka, Effects of states of carbon and solute nitrogen on toughness of ferritic steel, ISIJ Int. 63 (2023) 1054–1065, https://doi.org/10.2355/isijinternational.ISIJINT-2023-027.
[52] A. Sanchez-Navas, Sequential kinetics of a muscovite-out reaction: a natural example, Am. Mineral. 84 (1999) 1270–1286, https://doi.org/10.2138/am-1999-0905.
[53] B. Mishra, A. Mukhopadhyay, R. Sarkar, M.K. Kumawat, V. Madhu, M.J.N. V. Prasad, Strain hardening and stored energy in high-Mn austenitic based low-density steel, Mater. Sci. Eng. A 861 (2022) 144331, https://doi.org/10.1016/j.msea.2022.144331.
[54] S. Li, D. Li, H. Lu, P. Cao, R. Xie, Effect of κ carbides on deformation behavior of Fe-27Mn-10Al-1C low density steel, Crystals 12 (2022) 991, https://doi.org/10.3390/cryst12070991.
[55] H. Ohtani, M. Yamano, M. Hasebe, Thermodynamic analysis of the Fe-Al-C ternary system by incorporating ab initio energetic calculations into the CALPHAD approach, ISIJ Int. 44 (2004) 1738–1747, https://doi.org/10.2355/ISIJINTERNATIONAL.44.1738.
[56] K. Zhong, R. Bu, F. Jiao, G. Liu, C. Zhang, Toward the defect engineering of energetic materials: a review of the effect of crystal defects on the sensitivity, Chem. Eng. J. 429 (2022) 132310, https://doi.org/10.1016/j.cej.2021.132310.
[57] W. Mottay, P. Maugis, M. Jouiad, F. Roch, C. Perrin-Pellegrino, K. Hoummada, Effect of dislocation density on competitive segregation of solute atoms to dislocations, Mater. Sci. Eng. A 881 (2023) 145380, https://doi.org/10.1016/j.msea.2023.145380.
[58] T. Kawakubo, T. Nagira, K. Ushioda, H. Fujii, Friction stir welding of high phosphorus weathering steel-weldabilities, microstructural evolution and mechanical properties, ISIJ Int. 61 (2021) 2150–2158, https://doi.org/10.2355/isijinternational.ISIJINT-2021-007.
[59] C.A. Wert, Diffusion coefficient of C in α-iron, Phys. Rev. 79 (1950) 601–605, https://doi.org/10.1103/PhysRev.79.601.
[60] M. Soleimani, H. Mirzadeh, C. Dehghanian, Phase transformation mechanism and kinetics during step quenching of st37 low carbon steel, Mater. Res. Express 6 (2019) 1165f2, https://doi.org/10.1088/2053-1591/ab4960.
[61] M.A. Verzhakovskaya, S.S. Petrov, A.V. Pokoev, Heterodiffusion of aluminum in a-iron in a pulsed magnetic field, Tech. Phys. Lett. 33 (2007) 961–963, https://doi.org/10.1134/S1063785007110211.
[62] Y. Minamino, T. Yamane, S. Nakagawa, H. Araki, K. Hirao, Atomic size effect in interdiffusion of aluminum alloys, J. Jpn. Inst. Light Met. 37 (1987) 72–82, https://doi.org/10.2464/jilm.37.72.
[63] T. Kawakubo, K. Ushioda, H. Fujii, Grain boundary segregation and toughness of friction-stir-welded high-phosphorus weathering steel, Mater. Sci. Eng. A 832 (2022) 142350, https://doi.org/10.1016/j.msea.2021.142350.
[64] S. Liu, X. Li, X. Hu, X. Wang, F. Zhang, Y. Zhu, Characterization of microstructure and mechanical property evolutions of 42CrMo steel served at elevated temperatures, J. Mater. Eng. Perform. 33 (2024) 1732–1740, https://doi.org/10.1007/s11665-023-08108-9.
[65] S. Björklund, L.F. Donaghey, M. Hillert, The effect of alloying elements on the rate of Ostwald ripening of cementite in steel, Acta Metall. 20 (1972) 867–874, https://doi.org/10.1016/0001-6160(72)90079-X.
[66] T. Philippe, P.W. Voorhees, Ostwald ripening in multicomponent alloys, Acta Mater. 61 (2013) 4237–4244, https://doi.org/10.1016/j.actamat.2013.03.049.